

See discussions, stats, and author profiles for this publication at: <https://www.researchgate.net/publication/227997476>

# Design and Synthesis of Hierarchical Nanowire Composites for Electrochemical Energy Storage

ARTICLE *in* ADVANCED FUNCTIONAL MATERIALS · NOVEMBER 2009

Impact Factor: 11.81 · DOI: 10.1002/adfm.200900971

CITATIONS

190

READS

720

9 AUTHORS, INCLUDING:



**Zheng Chen**

Stanford University

34 PUBLICATIONS 1,022 CITATIONS

SEE PROFILE



**Qiangfeng Xiao**

General Motors Company

18 PUBLICATIONS 656 CITATIONS

SEE PROFILE



**Xiaolei Wang**

University of California, Los Angeles

29 PUBLICATIONS 646 CITATIONS

SEE PROFILE



**Fei Wei**

Tsinghua University

402 PUBLICATIONS 11,075 CITATIONS

SEE PROFILE

# Design and Synthesis of Hierarchical Nanowire Composites for Electrochemical Energy Storage

By Zheng Chen, Yaochun Qin, Ding Weng, Qiangfeng Xiao, Yiting Peng, Xiaolei Wang, Hexing Li,\* Fei Wei,\* and Yunfeng Lu\*

Nanocomposites of interpenetrating carbon nanotubes and vanadium pentoxide ( $V_2O_5$ ) nanowires networks are synthesized via a simple in situ hydrothermal process. These fibrous nanocomposites are hierarchically porous with high surface area and good electric conductivity, which makes them excellent material candidates for supercapacitors with high energy density and power density. Nanocomposites with a capacitance up to 440 and 200  $F\ g^{-1}$  are achieved at current densities of 0.25 and 10  $A\ g^{-1}$ , respectively. Asymmetric devices based on these nanocomposites and aqueous electrolyte exhibit an excellent charge/discharge capability, and high energy densities of 16  $W\ h\ kg^{-1}$  at a power density of 75  $W\ kg^{-1}$  and 5.5  $W\ h\ kg^{-1}$  at a high power density of 3 750  $W\ kg^{-1}$ . This performance is a significant improvement over current electrochemical capacitors and is highly competitive with Ni–MH batteries. This work provides a new platform for high-density electrical-energy storage for electric vehicles and other applications.

## 1. Introduction

Electrochemical capacitors have recently been attracting significant interest because they can instantaneously provide a higher power density than batteries and a higher energy density than conventional dielectric capacitors. Such outstanding properties make them excellent candidates for hybrid electric vehicles, computers, mobile electric devices, and other applications.<sup>[1,2]</sup> Generally, an electrochemical capacitor may be operated based on the electrochemical double-layer capacitance (EDLC) formed along an electrode/electrolyte interface or a pseudocapacitance

resulted from a fast reversible faradic process of redox-active materials (e.g., metal oxides or conductive polymers). For an EDLC-based capacitor, the rapid charge/discharge process provides the capacitor with a high power density, yet the energy density is limited by its effective double-layer area. To date, a large number of large-surface-area materials, such as activated carbon, templated carbon, and carbon nanotubes (CNTs), have been extensively studied. Activated carbons, with surface areas from 1 000–2 500  $m^2\ g^{-1}$ , are the most commonly used materials and may provide a capacitance up to 320  $F\ g^{-1}$  at low potential scanning rate. However, the capacitance may drop dramatically at high scanning rates because of their tortuous pore structure and high microporosity.<sup>[3]</sup> The tem-

plated carbons, on the other hand, exhibit uniform pore geometry and larger pore size; however, they have not shown any significant improvement in either energy or power performance.<sup>[4]</sup> For comparison, multiwalled CNTs<sup>[5]</sup> show capacitances up to 135  $F\ g^{-1}$  and single-wall CNTs<sup>[6]</sup> show capacitances up to 180  $F\ g^{-1}$ , which are still low for an actual device application. Compared with the EDLC-based capacitors, pseudocapacitors based on transition metal oxides or conducting polymers, such as  $RuO_2$ ,<sup>[7]</sup>  $MnO_2$ ,<sup>[8]</sup>  $NiO$ ,<sup>[9]</sup>  $Co_3O_4$ ,<sup>[10]</sup>  $V_2O_5$ ,<sup>[11]</sup> and polyaniline,<sup>[12]</sup> may provide much higher specific capacitances, up to 1 000  $F\ g^{-1}$  of the active material. Nonetheless, their actual applications are still limited by high cost, low operation voltage, or poor rate capability, mostly because of inefficient mass transport or of slow faradic redox kinetics.

To design a better electrochemical capacitor with both high energy and power density, a common strategy is to construct a hybrid capacitor that integrates both electric double-layer capacitance and pseudocapacitance within a single electrode. For example, Sato et al. loaded ruthenium oxide onto activated carbon, resulting in a capacity of 308  $F\ g^{-1}$  at 7.1 wt% ruthenium loading and a low scanning rate of 2  $mV\ s^{-1}$ .<sup>[13]</sup> Dong et al. reported a composite of  $MnO_2$  and templated carbon with a capacitance of 156  $F\ g^{-1}$  at 20 wt%  $MnO_2$  loading and a scanning rate of 50  $mV\ s^{-1}$ , which is about two times of that of the constituent carbon.<sup>[14]</sup> Kim et al. dispersed ruthenium oxide nanoparticles on carboxylated CNTs and obtained a total capacitance of 304  $F\ g^{-1}$  at a  $RuO_2$  loading of 50 wt%.<sup>[15]</sup> Similarly, composites prepared by electrodepositing  $MnO_2$  on vertically aligned CNT arrays exhibit

[\*] Prof. H. Li  
Department of Chemistry  
Shanghai Normal University  
Shanghai 200234 (China)  
E-mail: hexing-li@shnu.edu.cn

Prof. F. Wei  
Department of Chemical Engineering  
Tsinghua University  
Beijing 100084 (China)  
E-mail: wf-dce@tsinghua.edu.cn

Prof. Y. Lu, Z. Chen, Y. Qin, D. Weng, Q. Xiao, Y. Peng, X. Wang  
Department of Chemical and Biomolecular Engineering  
University of California  
Los Angeles, CA 90095 (USA)  
E-mail: luucla@ucla.edu

DOI: 10.1002/adfm.200900971

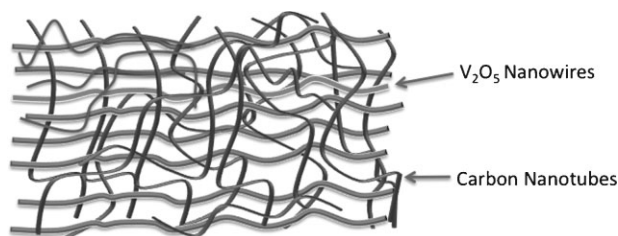
a capacitance up to  $199 \text{ F g}^{-1}$  (or  $305 \text{ F cm}^{-3}$ ) with a long cycle life; however, the complex fabrication process may limit their actual use.<sup>[16]</sup>

In spite of extensive research efforts, making supercapacitors with high energy and power densities still remains challenging. Herein, we report the synthesis of novel supercapacitor materials based on composites of low-cost, interpenetrating CNTs and  $\text{V}_2\text{O}_5$  nanowires, as illustrated in Scheme 1. This unique architecture provides several major advantages: i) the small dimension of the CNTs and the nanowires provide high surface areas, leading to a high EDLC and better utilization of the  $\text{V}_2\text{O}_5$  active sites (i.e., higher specific pseudocapacitance); ii) the interpenetrating nanotube/nanowire structure creates hierarchical porous channels, enabling effective electrolyte transport and active-site accessibility; iii) the nanowires are intimately intertwined with highly conductive CNTs, facilitating faster electron transport and more efficient current collection. Experimentally, these novel composites were readily synthesized using a one-pot hydrothermal approach. Briefly, multiwall CNTs were first modified to attach carboxylic groups on the surface. The hydrothermal reaction of vanadium oxide precursors in the presence of the modified CNTs led to the formation of the composites. Note that  $\text{V}_2\text{O}_5/\text{CNT}$  composites have been prepared by depositing a thin layer of  $\text{V}_2\text{O}_5$  (6-nm thick) on a CNT film, exhibiting a high Li ion capacitance of up to  $910 \text{ F g}^{-1}$  at a scan rate of  $10 \text{ mV s}^{-1}$ .<sup>[17]</sup> However, such composite thin films with extremely low  $\text{V}_2\text{O}_5$  loadings may not be suitable for practical applications. This work provides a simple but effective synthesis route and structure design towards better supercapacitors.

## 2. Results and Discussion

### 2.1. Characterization of the $\text{V}_2\text{O}_5$ Nanowire/CNT Composites

To systematically study the structure of the composites, we first studied the structure and morphology of the CNTs and the  $\text{V}_2\text{O}_5$  nanowires. Figure 1A and B show, respectively, representative scanning electron microscopy (SEM) and transmission electron microscopy (TEM) images of the CNTs, revealing a porous network of entangled CNTs with diameters of around 20–30 nm and lengths up to the micrometer scale. Similarly, the diameter of the  $\text{V}_2\text{O}_5$  nanowires is around 20–50 nm with lengths up to tens of micrometers (SEM image, Fig. 1C). A high-resolution TEM image (Fig. 1D) indicates that the nanowires contain an ordered layered structure; the selective area electron diffraction (SAED) pattern (inset, Fig. 1D) suggests that they are single crystalline. In situ growth of the  $\text{V}_2\text{O}_5$  nanowires within the porous CNT networks led to the formation of flexible, dark-brown nanocomposites (see the



**Scheme 1.** Schematic of method to form supercapacitor material based on interpenetrating networks of CNTs and  $\text{V}_2\text{O}_5$  nanowire.

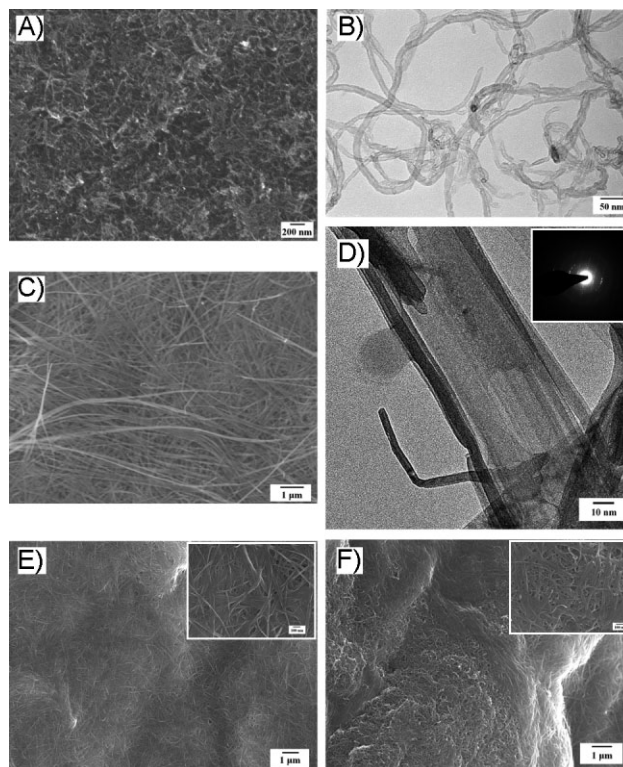


**Figure 1.** A) SEM and B) TEM images of the modified CNTs. C) SEM and D) TEM images and selective area electron diffraction (SAED, inset) of the  $\text{V}_2\text{O}_5$  nanowires. SEM images of CVC-2 E) before and F) after etching showing an interpenetrating structure.

Supporting Information, Fig. S1a), in which the  $\text{V}_2\text{O}_5$  loading can be readily controlled by tuning the ratio of CNTs to the  $\text{V}_2\text{O}_5$  precursor. Figure 1E shows an SEM image of a representative composite with 33 wt% CNTs (CVC-2), showing a continuous fibrous structure with pores up to micrometers in diameter.

Figure 2A shows nitrogen sorption isotherms of the CNTs,  $\text{V}_2\text{O}_5$  nanowires, and CVC-2, all of which are similar in shape. The CNTs show a surface area of  $150 \text{ m}^2 \text{ g}^{-1}$ , pore volume of  $0.488 \text{ cm}^3 \text{ g}^{-1}$ , and an average pore diameter of 12.5 nm (Fig. 2B). The  $\text{V}_2\text{O}_5$  nanowires show a lower surface area of  $83 \text{ m}^2 \text{ g}^{-1}$ , larger pore diameter of 26.7 nm, and a pore volume  $0.552 \text{ cm}^3 \text{ g}^{-1}$ . The CVC-2 exhibits a comparable surface area of  $125 \text{ m}^2 \text{ g}^{-1}$  and average pore size of 15.2 nm, suggesting the composite is hierarchically porous. The composites with different CNT loadings show similar porous fibrous structures (see Table 1 and the Supporting Information, Fig. S2); the morphology of the composites with higher CNT content is generally less uniform with more CNTs exposed on the surface. Such a hierarchical structure is essential to ensure a good capacitance performance, since the large pore channels allow rapid electrolyte transport, while the small ones provide the composites with higher surface areas and more surface active sites.

Furthermore, in situ growth of the nanowires within the CNT network leads to an interpenetrating network structure. X-ray diffraction (XRD; see Fig. 3) indicates that the free-growth  $\text{V}_2\text{O}_5$  nanowires are highly crystalline with well-defined (001) reflections at  $2\theta$  angles of  $9.1^\circ$ ,  $13.5^\circ$ ,  $25.5^\circ$ ,  $32.5^\circ$ , and  $42.0^\circ$ , consistent with the lamellar structure shown in Figure 1D. The CVC-2 composites

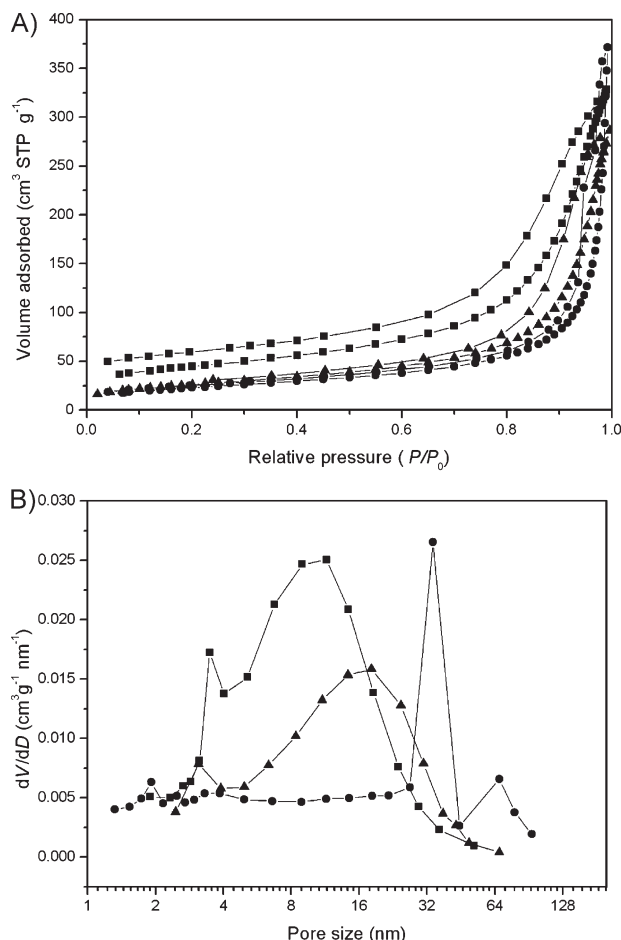


**Figure 2.** A) Nitrogen sorption isotherms and B) pore-size distributions of CNTs (■), V<sub>2</sub>O<sub>5</sub> nanowires (●), and CVC-2 (▲).

show similar reflections but with significantly lower intensity, indicating that the nanowires grown within the composites contain smaller crystalline domains. Partial removal of the nanowires using 1 wt% HF solution exposed the constituent CNT networks on the composite surface (Fig. 1F), further confirming the interpenetrating network structure. Such an interpenetrating network structure creates intimate contact of the CNT and nanowire networks, enabling rapid charge transport to the current collector through the highly conductive CNT network.

**Table 1.** Surface area, pore volume and pore size of the CNTs, V<sub>2</sub>O<sub>5</sub> nanowires, and their composites.

Sample	Surface area	Pore volume	Average pore size
	[m <sup>2</sup> g <sup>-1</sup> ]	[cm <sup>3</sup> g <sup>-1</sup> ]	[nm]
CNTs	156	0.488	12.5
CVC-1	108	0.639	20.9
CVC-2	125	0.445	15.2
CVC-3	144	0.645	17.8
CVC-4	142	0.486	13.7
V <sub>2</sub> O <sub>5</sub> nanowire	83	0.552	26.7

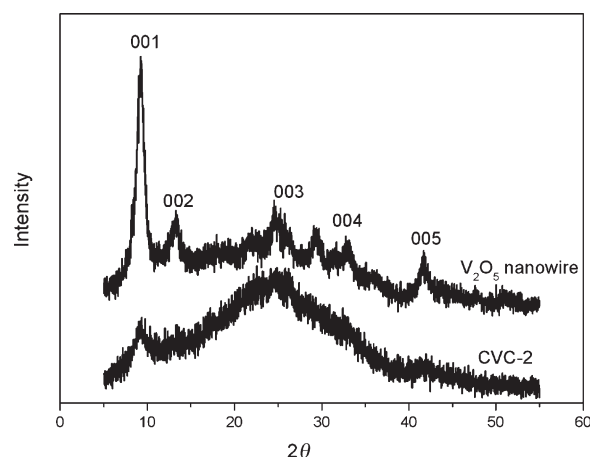


**Figure 3.** XRD patterns of the V<sub>2</sub>O<sub>5</sub> nanowires and CVC-2 composite.

## 2.2. Electrochemical Testing of V<sub>2</sub>O<sub>5</sub> Nanowire/CNT Composites

Such a unique hierarchical architecture endows the composites with high capacitance and rate capability. Figure 4 shows cyclic voltammograms (CVs) of the CNT, nanowire, and CVC-2 electrodes. The CNT electrode shows vague peaks at 0.12 and 0.05 V, which are attributed to the anodic oxidation and cathodic reduction of the surface carboxyl groups, respectively.<sup>[18]</sup> The nanowire electrode shows two broad peaks of anodic oxidation (0.50 and -0.05 V) and reduction (0.35 and -0.10 V), which are typical of the crystalline V<sub>2</sub>O<sub>5</sub>.<sup>[11]</sup> For comparison, the composite electrode shows a rectangular-shaped CV curve with a much larger area indicating a much higher capacitance. Furthermore, the redox peaks (anodic peaks at 0.51, -0.10, and -0.40 V, and cathodic peaks at 0.37, -0.28, and -0.42 V) are much better defined, suggesting a more pronounced contribution of redox capacitance to the overall capacitance.<sup>[19]</sup> Such three-redox pairs are rare in a V<sub>2</sub>O<sub>5</sub>-Na<sub>2</sub>SO<sub>4</sub> aqueous electrolyte system, which may be due to the ion (e.g., Na<sup>+</sup>) insertion and de-insertion reactions at different energy states.<sup>[20]</sup> Moreover, as shown in Figure 4c, the current of

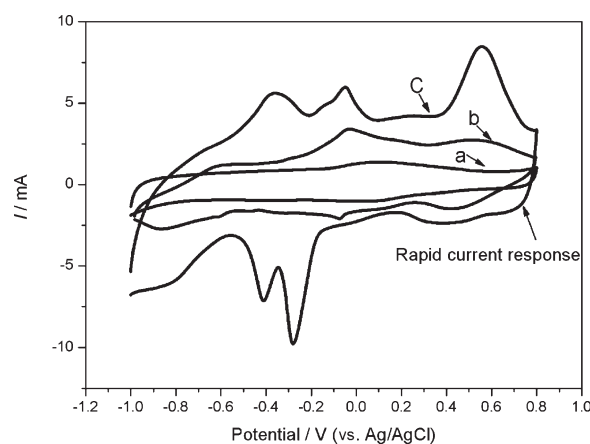


**Figure 4.** Cyclic voltammograms (CV) of CNT (a), V<sub>2</sub>O<sub>5</sub> nanowire (b) and CVC-2 (c) electrodes at a scanning rate of 10 mV s<sup>-1</sup> in 1 M Na<sub>2</sub>SO<sub>4</sub> aqueous solution at room temperature.



the nanocomposite electrode responds to the switching potential rapidly, particularly at the potential switching point of 0.8 V, indicating the composite electrode exhibits a lower equivalent series resistance (ESR) than that of the nanowire electrode. A small ESR is vital to achieve a high rate capability and power density, since the maximum power density ( $P_{\max}$ ) of a capacitor is generally determined by  $P_{\max} = V_i^2/4R$ , where  $V_i$  is the initial voltage and  $R$  is the ESR from the electrode materials, the electrolyte, and the contact resistance between electrode and current collector.

To further quantify their specific capacitance, galvanostatic charge–discharge curves were measured in the same working cells. Figure 5 shows the charge–discharge curves of the CNT, nanowire, and CVC-2 electrodes at a current density of  $1 \text{ A g}^{-1}$ . The CNT electrode shows a nearly linear charge–discharge curve, an indication of an ideal EDLC behavior with a specific capacitance of  $75 \text{ F g}^{-1}$ . The nanowire electrode shows similar charge–discharge curves with a slightly increased curvature, indicating that EDLC is still the primary contribution to the overall capacitance, which is  $146 \text{ F g}^{-1}$ . Note that although  $\text{V}_2\text{O}_5$  may provide a pseudocapacitance as high as  $530 \text{ F g}^{-1}$ , poor conductivity of the nanowires may attribute to the poor use of its pseudocapacitance. Intimately weaving these poorly conductive nanowires along with the highly conductive CNTs into the composites led to dramatically increased capacitances. Indeed, the charge–discharge plots of the composite electrode displays a pronounced transition between the two linear ranges, indicating contributions to the capacitance from both EDLC and pseudocapacitance. The specific capacitance calculated is around  $313 \text{ F g}^{-1}$ , which is significantly higher than that of the CNTs ( $75 \text{ F g}^{-1}$ ) and the  $\text{V}_2\text{O}_5$  nanowires ( $146 \text{ F g}^{-1}$ ). Since the surface area of the composite ( $125 \text{ m}^2 \text{ g}^{-1}$ ) is less than that of the CNTs ( $150 \text{ m}^2 \text{ g}^{-1}$ ), such a high capacitance can be attributed to the synergistic effect of the composite constituents with the unique hierarchical structure. Considering that the energy density of a capacitor is generally determined by  $E = CV_i^2/2$ , where  $C$  is the capacitance, composites with high capacitance are of great interest for high-energy-density device applications. To the best of our knowledge, although still lower than those of high-cost ruthenic oxide or ruthenic acid based supercapacitors, this is the highest capacitance reported among the macroscopic  $\text{V}_2\text{O}_5$ -<sup>[11]</sup> and  $\text{MnO}_2$ -based supercapacitors.<sup>[8,14,16]</sup>

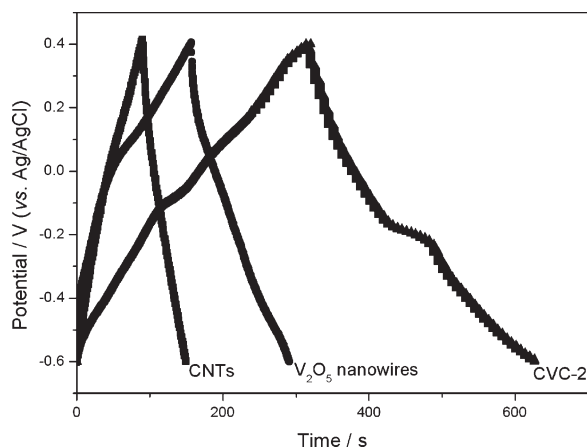


**Figure 5.** Galvanostatic charge–discharge curves of CNTs,  $\text{V}_2\text{O}_5$  nanowires, and CVC-2 electrodes at a charge–discharge current density of  $1 \text{ A g}^{-1}$ .

To further quantify their rate performance, CV studies at different scanning rates were conducted. Figure 6 shows CV curves of the CNT,  $\text{V}_2\text{O}_5$  nanowire, and CVC-2 electrodes at scanning rates from 5 to  $100 \text{ mV s}^{-1}$ . Due to its excellent conductivity and porous structure, the CNT electrode shows excellent power performance,<sup>[5]</sup> as shown by the rectangular shape of its CV curves at high scanning rates (see Fig. 6A). Consistent with its poor conductivity, the nanowire electrode shows a poor rate capability, as

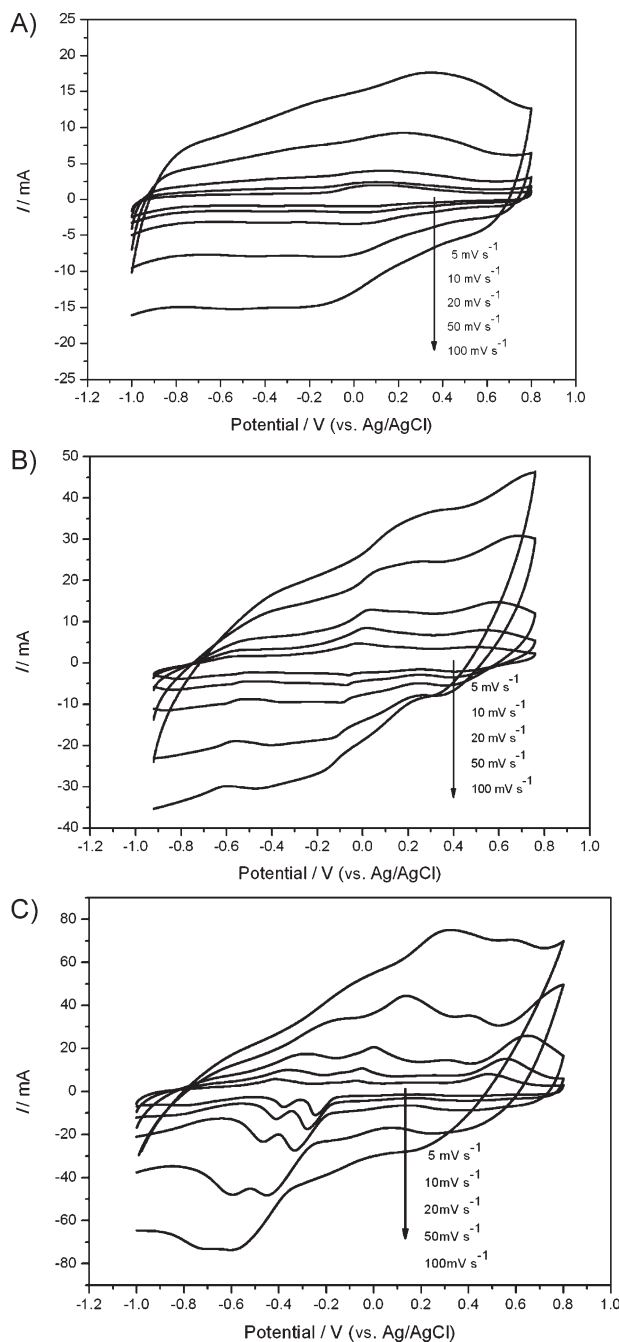


**Figure 6.** CV curves of A) the CNT, B) the  $\text{V}_2\text{O}_5$  nanowire, and C) the CVC-2 electrodes at various potential scanning rates from 5 to  $100 \text{ mV s}^{-1}$  in  $1 \text{ M Na}_2\text{SO}_4$  aqueous solution at room temperature.

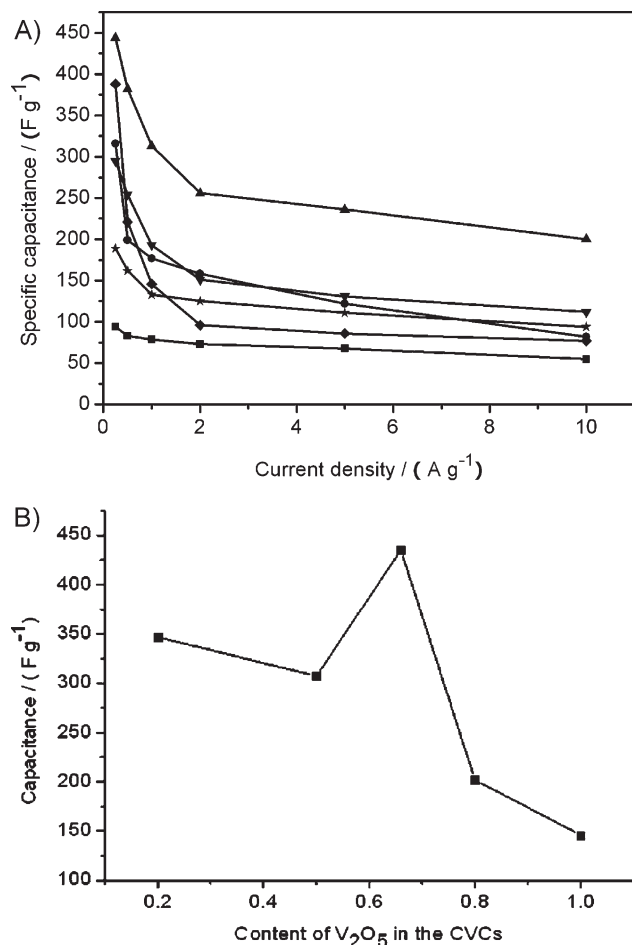


**Figure 7.** A) Gravimetric capacitance of the composite electrodes with different CNT content at different current densities: CNT electrode (■), V<sub>2</sub>O<sub>5</sub> nanowire electrode (◆), CVC-1 (●), CVC-2 (▲), CVC-3 (▼), and CVC-4 (★). B) Dependence of V<sub>2</sub>O<sub>5</sub>-based specific capacitances of the composites on the V<sub>2</sub>O<sub>5</sub> content at a current density of 1 A g<sup>-1</sup>.

shown by its highly distorted CV curves at high scanning rates (Fig. 6B). As expected, the CV curves of the composite electrode CVC-2 maintain the rectangular shape even at high scanning rates (Fig. 6C), which is more pronounced for the composites with higher CNT content (see the Supporting Information, Fig. S3). Compared with the CV curves of the CNT electrode, the slight shape distortion is due to the overlapping effect of the two different energy-storage mechanisms; nevertheless, this study fully confirms the excellent rate performance of the composites.

In short, the unique composite structure integrates the high rate performance of the CNT constituent with the high capacitance of the V<sub>2</sub>O<sub>5</sub> constituent, leading to the synergic energy storage materials. Nevertheless, CNTs have low energy density and V<sub>2</sub>O<sub>5</sub> has poor rate performance; optimization of the composition is therefore essential for good capacitance performance. Figure 7A compares the overall specific capacitance to the current density of the composites with different CNT content. The CVC-2 electrode shows the highest specific capacitance at different current densities. It affords a capacitance of 440 F g<sup>-1</sup> at a current density of 0.25 A g<sup>-1</sup> and preserves about 50% capacitance retention

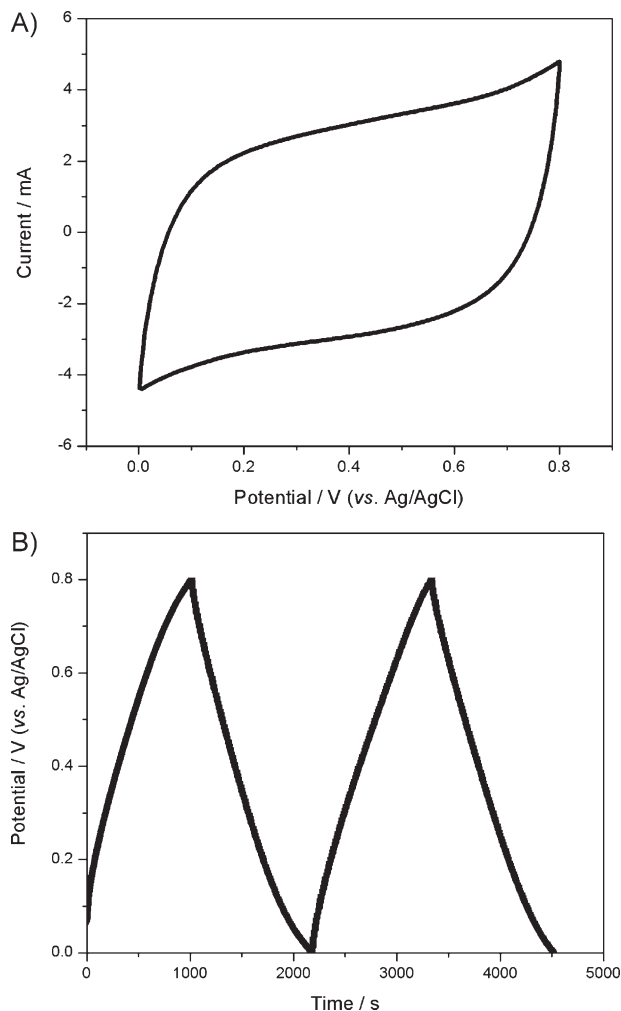


**Figure 8.** A) CV curves of mesoporous-carbon-supported MnO<sub>2</sub> (MnO<sub>2</sub>/C) at a scanning rate of 10 mV s<sup>-1</sup> in 1 M aqueous Na<sub>2</sub>SO<sub>4</sub> solution. B) Galvanostatic charge-discharge curves of MnO<sub>2</sub>/C at a current density of 0.1 A g<sup>-1</sup> at room temperature.

(200 F g<sup>-1</sup>) even at a current density of 10 A g<sup>-1</sup>. For comparison, the CNT electrode shows more than 60% capacitance retention at the same condition; however, its overall capacitance is low (55 F g<sup>-1</sup> at a current density of 10 A g<sup>-1</sup>). Similarly, although the V<sub>2</sub>O<sub>5</sub> nanowire electrode shows a high capacitance at low discharge rates (e.g., 388 F g<sup>-1</sup> at a current density of 0.25 A g<sup>-1</sup>), only 20% of the capacitance is retained at a current density of 10 A g<sup>-1</sup>, showing a poor rate capability. Figure 7B illustrates the V<sub>2</sub>O<sub>5</sub>-based specific capacitances of the composites versus the V<sub>2</sub>O<sub>5</sub> content at a current density of 1 A g<sup>-1</sup>. The composite electrodes consistently show much higher specific capacitance than that of the pure V<sub>2</sub>O<sub>5</sub> electrode, indicating that the CNT scaffold indeed facilitates the harvest of the V<sub>2</sub>O<sub>5</sub> pseudocapacitance. The CVC-2 electrode exhibits the highest overall capacitance and V<sub>2</sub>O<sub>5</sub>-based specific capacitance. This charge-discharge behavior is very consistent with the results from the cyclic voltammograms, further suggesting that improving conductivity of capacitor materials is essential when designing better electrochemical capacitors.

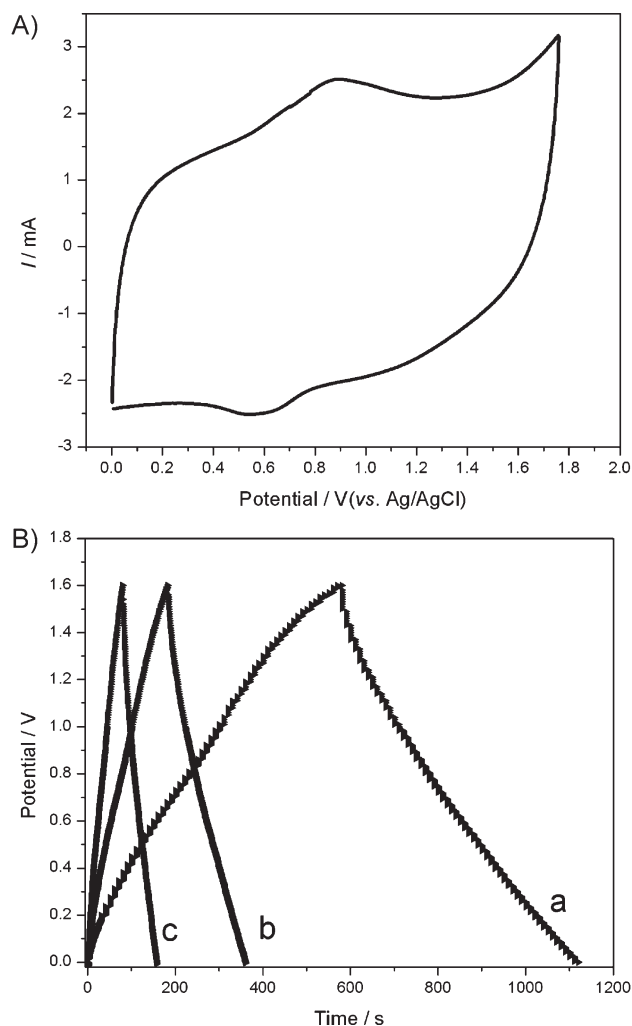


**Figure 9.** A) CV curve of an asymmetric supercapacitor with CVC-2 as anode and  $\text{MnO}_2/\text{C}$  as cathode at a scanning rate of  $10 \text{ mV s}^{-1}$ . B) Galvanostatic charge-discharge of the asymmetric supercapacitor at different current densities (a:  $0.64 \text{ mA cm}^{-2}$ , b:  $3.2 \text{ mA cm}^{-2}$ , and c:  $6.4 \text{ mA cm}^{-2}$ ) in  $1 \text{ M}$  aqueous  $\text{Na}_2\text{SO}_4$  solution at room temperature.

### 2.3. Device Application of $\text{V}_2\text{O}_5$ Nanowire/CNT Composites

To further evaluate these nanocomposites for real device application, we assembled an asymmetric supercapacitor using CVC-2 as the anode and  $\text{MnO}_2/\text{carbon}$  composite as the cathode (see the Experimental Section for details of the preparation of the  $\text{MnO}_2/\text{C}$  electrode). The typical cyclic voltammogram of the  $\text{MnO}_2/\text{C}$  electrode are shown in Figure 8A. The rectangular-shaped CV plot indicates ideal capacitive behavior of the electrode. Galvanostatic charge-discharge curves of the  $\text{MnO}_2/\text{C}$  electrode at a current density of  $0.1 \text{ A g}^{-1}$  reveal that the electrode material can provide a specific capacitance of  $145 \text{ F g}^{-1}$ , as calculated from Figure 8B.

For the asymmetric supercapacitor consisting of the CVC-2 and  $\text{MnO}_2/\text{C}$  electrodes, an ideal capacitive behavior was observed from  $0$ – $1.6 \text{ V}$  in  $1 \text{ M}$   $\text{Na}_2\text{SO}_4$  (Fig. 9). A capacitance of  $45 \text{ F g}^{-1}$  (based on the total weight of the anode and cathode materials) was achieved at a discharge current density of  $0.64 \text{ mA cm}^{-2}$ , corresponding to an energy density of

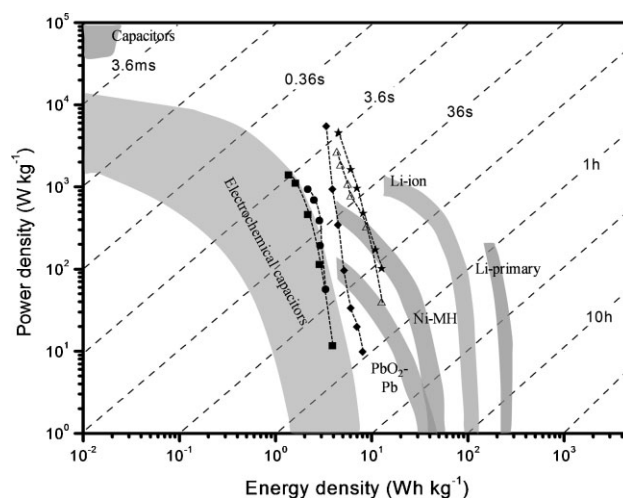


**Figure 10.** Ragone plot of the asymmetric supercapacitor (★) consisting of a CVC-2 anode and  $\text{MnO}_2/\text{carbon}$  cathode in comparison with carbon-based supercapacitors from active carbon (■) [21], mesoporous carbon CMK-3 (●) [22], hierarchical porous graphitic carbon (◆) [23], and phosphorus-enriched carbon (△) [24].

$16 \text{ W h kg}^{-1}$  at a power density of  $75 \text{ W kg}^{-1}$ . The device still possesses an energy density of  $5.5 \text{ W h kg}^{-1}$  even at a power density of  $3750 \text{ W kg}^{-1}$  and retains more than 90% of the initial capacitance after 100 cycles of charge and discharge, indicative of high power performance and good cycling stability. Figure 10 shows the Ragone plot derived from the constant-current charges and discharges (Fig. 9B) of the asymmetric supercapacitor, in comparison with some advanced aqueous-based supercapacitors from the recent literature. The energy and power performance of this asymmetric supercapacitor are highly competitive with Ni-MH batteries and significantly improved over current electrochemical capacitors. Considering the specific capacitance of the cathode materials ( $\text{MnO}_2/\text{C}$ ) is below  $150 \text{ F g}^{-1}$  (Fig. 8B), an even higher energy density could be realized if a better cathode material were available. Moreover, considering that the CNT,  $\text{V}_2\text{O}_5$  precursor, and processing can be achieved at a cost comparable to that of traditional carbon-based devices, these composites hold great promise as next generation electrical energy storage materials.

## 3. Conclusions

In summary, we have developed a class of supercapacitor composites based on confined growth of  $\text{V}_2\text{O}_5$  nanowires within a conductive porous CNT scaffold. The hierarchically porous, interpenetrating network structure provides the composites with high capacitance and excellent rate performance. This design concept can be generalized towards other capacitor composites containing other low-dimensional metal oxides, such as  $\text{MnO}_2$ ,  $\text{Co}_3\text{O}_4$  and  $\text{NiO}$ , opening a new avenue for a large spectrum of device applications.

## 4. Experimental Section

**Synthesis of the CNT/ $\text{V}_2\text{O}_5$  Composites:** Multi-wall carbon nanotubes (CNTs) were functionalized by attaching carboxylic groups on the surface using a method similar to that developed by Gao et al. [25]. Briefly,

pristine CNTs (12.0 g), HNO<sub>3</sub> (65%, 100 mL), and H<sub>2</sub>SO<sub>4</sub> (98%, 300 mL) were mixed in a flask and vigorously stirred under reflux for 100 min. The mixture was diluted with deionized water, filtered, and re-dispersed in water. This process was repeated until the pH of the filtrate was around neutral. Then, modified CNTs were dried in a vacuum oven for 24 h at 80 °C. A hydrothermal method similar to that of Xiong et al. [26] was used to synthesize the composites. Briefly, appropriate amount of the modified CNTs, HCl (2 M, 0.5 mL), ammonium metavanadate (NH<sub>4</sub>VO<sub>3</sub>, 0.15 g), and surfactant P123 (EO<sub>20</sub>PO<sub>70</sub>EO<sub>20</sub>, where EO and PO are ethylene oxide and propylene oxide, respectively; 0.25 g) were mixed under ultrasonication for 10 min. After stirring for 1 h, the mixtures were transferred to a 20 mL Teflon-lined autoclave and heated to 120 °C for 24 h. The resulted precipitates were filtered and rinsed with water and acetone several times and dried at 80 °C for 12 h under vacuum. The amounts of CNTs used were 0.037, 0.078, 0.15, to 0.6 g, resulting in composites with 20, 33, 50, and 67 wt% of the CNTs, which were denoted as CVC-1, CVC-2, CVC-3, and CVC-4, respectively.

**Synthesis of Mesoporous-Carbon-Supported MnO<sub>2</sub> (MnO<sub>2</sub>/C):** Mesoporous carbon was synthesized according to the method reported by Pang et al. [27], using sucrose as the carbon source and silica clusters and colloids as the template. Growth of MnO<sub>2</sub> onto the mesoporous carbon was realized according to the method reported by Long and co-workers [28]. Simply, as-prepared mesoporous carbon (0.1 g) was soaked into a flask containing KMnO<sub>4</sub> aqueous solution (0.1 M, 100 mL) under vacuum for 10 min. The mixture was stirred at 50 °C for 2 h for direct growth of MnO<sub>2</sub> onto the carbon surface. After reaction, the as-derived powder was washed by deionized water several times and dried at vacuum at 80 °C for 12 h.

**Material and Electrode Characterization:** X-ray diffraction measurements were taken on a Panalytical X'Pert Pro X-ray powder diffractometer using Cu-K $\alpha$  radiation ( $\lambda = 1.54 \text{ \AA}$ ). Nitrogen sorption isotherms were measured at 77 K with a Micromeritics ASAP 2020 analyzer. The samples were degassed in vacuum at 180 °C for 3 h. The specific surface areas ( $S_{\text{BET}}$ ) were calculated by the Brunauer–Emmett–Teller (BET) method using adsorption branch in a relative pressure range from 0.04 to 0.25. The pore size distributions ( $D_p$ ) were derived from the adsorption branches of isotherms using the Barrett–Joyner–Halenda (BJH) model. SEM experiments were conducted on a Jeol JSM-6700 FE-SEM instrument. TEM experiments were conducted on a Philips CM120 instrument operated at 120 kV.

The V<sub>2</sub>O<sub>5</sub> nanowire/CNT or MnO<sub>2</sub>/C composites were assembled onto foam nickel collectors to fabricate porous electrodes (see the photograph of V<sub>2</sub>O<sub>5</sub> nanowire/CNT electrode in the Supporting Information, Fig. S1b). Briefly, 80% of the testing materials, 10% carbon black, and 10% poly(vinylidene fluoride) (PVDF) dispersed in *N*-methylpyrrolidinone (NMP) were mixed to form slurries. The slurries were ultrasonically treated at 60 °C, coated on a nickel foam substrate, and dried at 80 °C for 10 min under vacuum. The as-formed electrodes were then pressed at a pressure of 2 MPa cm<sup>-2</sup> and further dried under vacuum at 100 °C for 12 h. The electrochemical measurements were conducted in a Princeton VMP3 electrochemistry workstation. Cyclic voltammetry measurements were conducted in 1 M Na<sub>2</sub>SO<sub>4</sub> aqueous solution at room temperature using a platinum wire as the counter electrode and an Ag/AgCl electrode as the reference electrode. The specific capacitance ( $C$ ) of the electrode materials were derived from  $C = I/(dE/dt) \approx I/(\Delta E/\Delta t)$ , where  $I$  is the constant discharge current density,  $E$  is cell voltage, and  $dE/dt$  is slope of the discharge curve.

## Acknowledgements

This work was partially supported by ONR, NSF-CAREER, and Sandia National Laboratories. The authors are also thankful for the support from the CheungKong Scholar program. Supporting Information is available online from Wiley InterScience or from the author.

Received: June 3, 2009

Published online: September 28, 2009

- [1] B. E. Conway, *Electrochemical Supercapacitors, Scientific Fundamentals and Technological Applications*, Kluwer Academic/Plenum, New York 1999.
- [2] J. R. Miller, A. F. Burke, *Electrochem. Soc. Interface* **2008**, 17, 53.
- [3] a) T. A. Centeno, F. Stoeckli, *J. Power Source* **2006**, 154, 314. b) E. Frackowiak, *Phys. Chem. Chem. Phys.* **2007**, 9, 1774.
- [4] a) K. Jurewicz, C. Vix-Guterl, E. Frackowiak, S. Saadallah, M. Reda, J. Parmentier, J. Patarin, F. Béguin, *J. Phys. Chem. Solids* **2004**, 65, 287. b) A. B. Fuentès, G. Lota, T. A. Centeno, E. Frackowiak, *Electrochim. Acta* **2005**, 50, 2799. c) H. Q. Li, R. L. Liu, D. Y. Zhao, Y. Y. Xia, *Carbon* **2007**, 45, 2628.
- [5] a) C. S. Du, N. Pan, *Nanotechnology* **2006**, 17, 5314. b) G. Lota, K. Lota, E. Frackowiak, *Electrochem. Commun.* **2007**, 9, 1828.
- [6] a) K. H. An, W. S. Kim, Y. S. Park, Y. C. Choi, S. M. Lee, D. C. Chung, D. J. Bae, S. C. Lim, Y. H. Lee, *Adv. Mater.* **2001**, 13, 497. b) D. N. Futaba, K. Hata, T. Yamada, T. Hiraoka, Y. Hayamizu, Y. Kakudate, O. Tanaïke, H. Hatori, M. Yumura, S. Iijima, *Nat. Mater.* **2006**, 5, 987.
- [7] a) J. P. Zheng, P. J. Cygan, T. R. Jow, *J. Electrochem. Soc.* **1995**, 142, 2699. b) C. C. Wang, C. C. Hu, *Electrochim. Acta* **2005**, 50, 2573. c) V. Subramanian, S. C. Hall, P. H. Smith, B. Rambabu, *Solid State Ionics* **2004**, 175, 511.
- [8] a) S. C. Pang, M. A. Anderson, T. W. Chapman, *J. Electrochem. Soc.* **2000**, 147, 444. b) M. Toupin, T. Brousse, D. Bélanger, *Chem. Mater.* **2004**, 16, 3184. c) M. Nakayama, T. Kanaya, R. Inoue, *Electrochem. Commun.* **2007**, 9, 1154. d) V. Subramanian, H. W. Zhu, B. Q. Wei, *J. Power Source* **2006**, 159, 361.
- [9] a) K. C. Liu, M. A. Anderson, *J. Electrochem. Soc.* **1996**, 143, 124. b) K. W. Nam, K. B. Kim, *J. Electrochem. Soc.* **2002**, 149, 346. b) J. W. Lang, L. B. Kong, W. J. Wu, Y. C. Luo, L. Kang, *Chem. Commun.* **2008**, 35, 4213.
- [10] C. Lin, J. A. Ritter, B. N. Popov, *J. Electrochem. Soc.* **1998**, 145, 4097.
- [11] a) R. N. Reddy, R. G. Reddy, *J. Power Sources* **2006**, 156, 700. b) Z. J. Lao, K. Konstantinov, Y. Tournaire, S. H. Ng, G. X. Wang, H. K. Liu, *J. Power Sources* **2006**, 162, 1451.
- [12] a) Y. G. Wang, H. Q. Li, Y. Y. Xia, *Adv. Mater.* **2006**, 18, 2619. b) S. R. Silvakumar, W. J. Kim, J. A. Choi, D. R. MacFarlane, M. Forsyth, D. W. Kim, *J. Power Sources* **2007**, 171, 1062.
- [13] Y. Sato, K. Yomogida, T. Nanaumi, K. Kobayakawa, Y. Ohsawa, M. Kawai, *Electrochem. Solid-State Lett.* **2000**, 3, 113.
- [14] X. P. Dong, W. H. Shen, J. L. Gu, L. M. Xiong, Y. F. Zhu, H. Li, J. Lin, Shi, *J. Phys. Chem. B* **2006**, 110, 6015.
- [15] I. H. Kim, J. H. Kim, Y. H. Lee, K. B. Kim, *J. Electrochem. Soc.* **2005**, 152, 2170.
- [16] H. Zhang, G. P. Cao, Z. Y. Wang, Y. S. Yang, Z. J. Shi, Z. N. Gu, *Nano Lett.* **2008**, 8, 2664.
- [17] I. H. Kim, J. H. Kim, B. W. Cho, Y. H. Lee, K. B. Kim, *J. Electrochem. Soc.* **2006**, 153, A989.
- [18] E. Frackowiak, *App. Phys. Lett.* **2000**, 77, 2421.
- [19] W. Sugimoto, H. Iwata, Y. Yasunaga, Y. Murakami, Y. Takasu, *Angew. Chem, Int. Ed.* **2003**, 42, 4092.
- [20] a) F. Huguenin, E. M. Giroto, G. Ruggeri, R. M. Torresi, *J. Power Sources* **2003**, 114, 133. b) M. Malta, G. Louarn, N. Errien, R. M. Torresi, *J. Power Sources* **2006**, 156, 533.
- [21] Y. G. Wang, Y. Y. Xia, *Electrochem. Commun.* **2005**, 7, 1138.
- [22] W. Xing, S. Z. Qiao, R. G. Ding, F. Li, G. Q. Lu, Z. F. Yan, H. M. Cheng, *Carbon* **2006**, 44, 216.
- [23] D. W. Wang, F. Li, M. Liu, G. Q. Lu, H. M. Cheng, *Angew. Chem, Int. Ed.* **2008**, 47, 373.
- [24] D. Hulicova-Jurcakova, A. M. Puziy, O. I. Poddubnaya, F. Suárez-García, J. M. D. Tascón, G. Q. Lu, *J. Am. Chem. Soc.* **2009**, 131, 5026.
- [25] C. Gao, C. D. Vo, Y. Z. Jin, W. W. Li, S. P. Armes, *Macromolecules* **2005**, 38, 8634.
- [26] C. R. Xiong, A. E. Aliev, B. Gnade, K. J. Balkus, Jr, *ACS Nano* **2008**, 2, 293.
- [27] J. B. Pang, Q. Y. Hu, Z. W. Wu, J. E. Hampsey, J. B. He, Y. F. Lu, *Microporous Mesoporous Mater.* **2004**, 74, 73.
- [28] A. E. Fischer, K. A. Pettigrew, D. R. Rolison, R. M. Stroud, J. W. Long, *Nano Lett.* **2007**, 7, 281.